Monthly Notices of the ROYAL ASTRONOMICAL SOCIETY

MNRAS **520,** 3066–3079 (2023)
Advance Access publication 2023 January 27

https://doi.org/10.1093/mnras/stad275

The vertical structure of the spiral galaxy NGC 3501: first stages of the formation of a thin metal-rich disc

Natascha Sattler,[1★] Francesca Pinna,[1] Nadine Neumayer,[1] Jesus Falcón-Barroso,[2,3] Marie Martig,[4] Dimitri A. Gadotti,[5,6] Glenn van de Ven[7] and Ivan Minchev[8]

[1]*Max-Planck-Institut für Astronomie, Königstuhl 17, D-69117 Heidelberg, Germany*
[2]*Instituto de Astrofísica de Canarias, Calle Via Láctea s/n, E-38200 La Laguna, Tenerife, Spain*
[3]*Departamento de Astrofísica, Universidad de La Laguna, Calle Astrofísico Francisco Sánchez s/n, E-38206 La Laguna, Tenerife, Spain*
[4]*Astrophysics Research Institute, Liverpool John Moores University, 146 Brownlow Hill, Liverpool L3 5RF, UK*
[5]*European Southern Observatory, Karl-Schwarzschild-Str 2, D-85748 Garching, Germany*
[6]*Centre for Extragalactic Astronomy, Department of Physics, Durham University, South Road, Durham DH1 3LE, UK*
[7]*Department of Astrophysics, University of Vienna, Türkenschanzstraße 17, A-1180 Vienna, Austria*
[8]*Leibniz Institut fur Astrophysik Potsdam (AIP), An der Sterwarte 16, D-14482 Potsdam, Germany*

Accepted 2023 January 23. Received 2023 January 12; in original form 2022 September 28

ABSTRACT

We trace the evolution of the edge-on spiral galaxy NGC 3501, making use of its stellar populations extracted from deep integral-field spectroscopy MUSE observations. We present stellar kinematic and population maps, as well as the star formation history, of the south-western half of the galaxy. The derived maps of the stellar line-of-sight velocity and velocity dispersion are quite regular, show disc-like rotation, and no other structural component of the galaxy. However, maps of the stellar populations exhibit structures in the mass-weighted and light-weighted age, total metallicity, and [Mg/Fe] abundance. These maps indicate that NGC 3501 is a young galaxy, consisting mostly of stars with ages between 2 and 8 Gyr. Also, they show a thicker more extended structure that is metal-poor and α-rich, and another inner metal-rich and α-poor one with smaller radial extension. While previous studies revealed that NGC 3501 shows only one morphological disc component in its vertical structure, we divided the galaxy into two regions: an inner metal-rich mid-plane and a metal-poor thicker envelope. Comparing the star formation history of the inner thinner metal-rich disc and the thicker metal-poor disc, we see that the metal-rich component evolved more steadily, while the metal-poor one experienced several bursts of star formation. We propose this spiral galaxy is being observed in an early evolutionary phase, with a thicker disc already in place and an inner thin disc in an early formation stage. So we are probably witnessing the birth of a future massive thin disc, continuously growing embedded in a preexisting thicker disc.

Key words: galaxies: evolution – galaxies: individual: NGC 3501 – galaxies: kinematics and dynamics – galaxies: spiral – galaxies: star formation – galaxies: structure.

1 INTRODUCTION

The vertical structure of external galaxies can be best studied when they are seen edge-on, where disc structures with different thicknesses can be identified. Thick and thin discs in external galaxies were already discovered and described many decades ago by Burstein (1979), and in the Milky Way by Gilmore & Reid (1983). Thick and thin discs have since then been identified in many more galaxies. For instance, Yoachim & Dalcanton (2006) analysed the vertical structure of 34 edge-on galaxies and found that 32 of them host a thick disc. In a further study of 141 galaxies by Comerón, Salo & Knapen (2018), 17 galaxies show only one distinct disc component, while 124 galaxies host at least two large-scale disc components, like a thin and thick disc.

In external galaxies, thick and thin discs are usually defined geometrically, after fitting vertical surface-brightness profiles as done in Comerón et al. (2018), or selecting stars far away from the mid-plane (e.g. Yoachim & Dalcanton 2008a). In this paper, we use this geometric definition of the thick disc: this is a component with a large scale height, made of stars with large excursions above the mid-plane, and high velocity dispersion. Such thick discs are usually significantly fainter and less massive than thin discs (Yoachim & Dalcanton 2006; Comerón et al. 2018).

Thick and thin discs also generally differ in their stellar populations: thick discs typically consist of stars that are older, more metal-poor, and more enhanced in α-elements than thin discs (e.g. Yoachim & Dalcanton 2008b; Comerón et al. 2015; Kasparova et al. 2016; Pinna et al. 2019b; Martig et al. 2021; Scott et al. 2021). However, thick and thin discs do not necessarily have strong differences in age, as can be seen in some lenticular galaxies in galaxy clusters (Comerón et al. 2016; Pinna et al. 2019a). For the Milky Way, while in the solar neighbourhood it is true that stars

★ E-mail: sattler@mpia.de

© The Author(s) 2023.
Published by Oxford University Press on behalf of Royal Astronomical Society. This is an Open Access article distributed under the terms of the Creative Commons Attribution License (https://creativecommons.org/licenses/by/4.0/), which permits unrestricted reuse, distribution, and reproduction in any medium, provided the original work is properly cited.

Downloaded from https://academic.oup.com/mnras/article/520/2/3066/7008533 by guest on 17 May 2023

at higher distances from the mid-plane are older, more metal-poor, and α-rich (Gilmore & Wyse 1985; Ivezić et al. 2008; Schlesinger et al. 2012; Casagrande et al. 2016), this does not hold everywhere in the disc. The geometric thick disc does not have a strong radial metallicity gradient (Cheng et al. 2012), but has a clear gradient in [α/Fe]: the outer thick disc mostly contains α-poor stars (Hayden et al. 2017; Queiroz et al. 2020; Gaia Collaboration 2022). A radial age gradient in the thick disc was also predicted by Minchev et al. (2015) and measured by Martig et al. (2016) with ∼9 Gyr old stars in the inner part of the disc and ∼5 Gyr old stars in the outer thick disc. Geometric thick discs can thus be complex components, reflecting the complexity and diversity in the star formation and assembly histories of their host galaxies.

There are two main pathways through which the stellar mass in a galaxy might be assembled: 'inside-out' and 'outside-in' formation (Sánchez-Blázquez et al. 2007; Pérez et al. 2013). Galaxies with a mass larger than $10^{10.5}$ $M_\odot$ (e.g. Pérez et al. 2013; Pan et al. 2015) grow from the 'inside-out', meaning that the stellar mass is first assembled in the central mid-plane. This central star formation, as well as gas inflow to a central supermassive black hole, can then quench the star formation in the centre by heating the cool gas from which new stars would be formed or by blowing it out (Schawinski et al. 2014). The star formation is then shifted to the outer parts of the galaxy, where gas is accreted from the intergalactic medium or satellites. This 'inside-out' scenario would then result in a negative age gradient, where older stars are located in the central region and younger stars in the galaxy outskirts (Pérez et al. 2013). Low-mass galaxies in contrast are more likely to form from an 'outside-in' process, resulting in a positive age gradient with younger stars in the centre and older stars in the outer regions (Gallart et al. 2008; Zhang et al. 2012).

Thin discs, with an extended star formation and long chemical enrichment making them α-poor and metal-rich, are thought to form mainly *in situ*. Both gas-rich galaxy mergers and accretion of gas from the intergalactic medium might play a key role in providing large amounts of gas to fuel the extended and massive star formation in thin discs (Gallart et al. 2019; Martig et al. 2021; Conroy et al. 2022).

Thick discs themselves can also be explained by many different processes. A thin disc can be dynamically heated by minor mergers (Quinn, Hernquist & Fullagar 1993; Abadi et al. 2003), or the thick disc can be made up of stars accreted from satellite galaxies. Another possible mechanism to form a thicker disc is proposed by Meng & Gnedin (2021), where a rapid change in the orientation of the mid-plane leads to a thickening of the disc. Alternatively, thick discs could be born already thick, following violent disc instabilities (Bournaud, Elmegreen & Martig 2009), or because of one or more gas-rich mergers (Brook et al. 2004), where the turbulent gas carries lower angular momentum leading to the thicker disc shape.

All these scenarios do not have to be mutually exclusive, and combinations of those were recently proposed (Pinna et al. 2019a, b; Martig et al. 2021). Minchev et al. (2015) also show that radial gradients in α abundance and age result from different formation channels for the inner and outer thick discs: the inner thick disc forms already thick at high redshift, while the outer thick disc progressively grows as younger populations are subjected to external perturbations. Those perturbations create some disc flaring and bring young, α-poor stars into the outer regions of geometric thick discs. Whether this picture proposed by Minchev et al. (2015) applies only to the Milky Way or to many other galaxies is still unclear: our general understanding is partly limited by the small amount of spectroscopic data available for external galaxies.

However, obtaining these properties with spectroscopic observations of thick discs is challenging, because of the fast drop in surface brightness when moving away from the mid-plane. A few studies have gathered long-slit observations (Yoachim & Dalcanton 2008a, b; Du et al. 2017; Katkov et al. 2019; Kasparova, Katkov & Chilingarian 2020) to measure the kinematic properties, as well as the stellar populations for thin and thick discs of several edge-on galaxies.

Nevertheless, using integral-field spectroscopy to continuously map stellar kinematics and populations is significantly more efficient. The first dedicated study of an edge-on galaxy using integral-field units was done by Comerón et al. (2015) on ESO 533–4 with VIMOS, but with a relatively poor spatial resolution. Then the first attempt using MUSE (Multi-Unit Spectroscopic Explorer) data was performed by Comerón et al. (2016), where the kinematics and stellar populations of a high-mass, edge-on S0 galaxy were studied. So far, there are very few studies in the literature using integral field spectroscopy and most of them focus on bright S0 galaxies (Comerón et al. 2016; Guérou et al. 2016; Pinna et al. 2019a, b). Due to low surface brightness, strong emission lines and dust, similar studies in late-type galaxies are significantly more challenging. Nevertheless, Comerón et al. (2019) obtained spatial resolved maps of the stellar kinematics of eight late-type galaxies, whereas Martig et al. (2021) and Scott et al. (2021) studied the spiral galaxies NGC 5746 and UGC 10738.

This paper extends this work by studying the stellar kinematics and populations, as well as the formation and evolution of the edge-on spiral galaxy NGC 3501. This galaxy was one out of the 17 galaxies from Comerón et al. (2018) whose vertical surface brightness profiles were fitted and showed only one disc component. This paper is structured as follows: First, we will give a brief overview of the target galaxy in Section 2, followed by a description of the observations and data reduction in Section 3, and the different analysis methods in Section 4. Then we present the results in Section 5, discuss them in Section 6, and finally give our conclusion in Section 7.

2 NGC 3501

NGC 3501 is an edge-on Scd galaxy with a boxy bulge (Lütticke, Dettmar & Pohlen 2000). Some properties of NGC 3501 are listed in Table 1, while Fig. 1 shows an SDSS *g*-band (Ahumada et al. 2020) and an S^4G 3.6 μm image (Sheth et al. 2010; Muñoz-Mateos et al. 2013; Querejeta et al. 2015). This spiral galaxy is with 1.5×10^{10} $M_\odot$ slightly less massive than the Milky Way (5.43×10^{10} $M_\odot$; McMillan 2017). It has a star formation rate of 0.52 $M_\odot$ yr^{-1} (Nersesian et al. 2019), which is slightly below the Milky Way star formation rate of 0.68–1.45 $M_\odot$ yr^{-1} (Robitaille & Whitney 2010).

Using 3.6 μm data from the S^4G survey (Sheth et al. 2010), Comerón et al. (2018) found that the vertical structure of the disc can be fitted by two components, a thin and a thick disc. However, the thick disc component always dominates for NGC 3501, so they proposed a single disc structure for this galaxy. This single thicker disc of NGC 3501 has a fitted scale height of 3.3 arcsec (0.37 kpc), while the fitted scale height of a thin disc for NGC 3501 is 1.0 arcsec (0.11 kpc) (Comerón et al. 2018). Therefore, the thicker disc of NGC 3501 is comparable in size to the Milky Ways thin disc, which has a scale height of 0.3 kpc (Jurić et al. 2008). And it is significantly thinner than the Milky Ways thick disc, which has a scale height of 0.9 kpc (Jurić et al. 2008).

Márquez et al. (2002) determined rotation curves and metallicity gradients using long-slit spectra in the region of Hα emission. The rotation curve of NGC 3501 showed a maximum rotation velocity

Downloaded from https://academic.oup.com/mnras/article/520/2/3066/7008533 by guest on 17 May 2023

Table 1. Properties of NGC 3501.

Property	Value	Comments	Reference
Type	Scd		Ann, Seo & Ha (2015)
RA	$11^{h}02^{m}47^{s}.307$	(J2000.0)	Skrutskie et al. (2006)
Dec.	$+17^{\circ}59'22''.31$	(J2000.0)	Skrutskie et al. (2006)
PA	28	(°)	Comerón et al. (2018)
Distance	23.55	(Mpc)	Tully, Courtois & Sorce (2016)
Redshift	0.00377		Haynes et al. (2018)
Major axis	233.4	D_{25} (arcsec)	de Vaucouleurs et al. (1991)
Minor axis	30.81	d_{25} (arcsec)	de Vaucouleurs et al. (1991)
Thick disc scale height	3.3	(arcsec)	Comerón et al. (2018)
Thin disc scale height	1.0	(arcsec)	Comerón et al. (2018)
Stellar mass	1.5	($\times 10^{10}$ $M_{\odot}$)	Sheth et al. (2010)
Dust mass	1.1	($\times 10^{7}$ $M_{\odot}$)	Nersesian et al. (2019)
v_c	136	(km s^{-1})	Sheth et al. (2010)

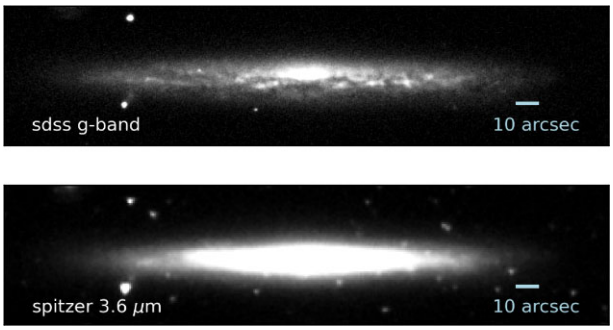

Figure 1. SDSS g-band image (Ahumada et al. 2020) of NGC 3501 at the top and S^4G 3.6 μm image (Sheth et al. 2010; Muñoz-Mateos et al. 2013; Querejeta et al. 2015) of NGC 3501 at the bottom.

of around 100 km s^{-1} within 100 arcsec of the centre with large errorbars of around 50 km s^{-1} in the outer regions.

Márquez et al. (2002) also found a negative radial metallicity gradient, as probed by [N II]/H α in H II regions. They also classified NGC 3501 as a mildly interacting spiral that shows non-disruptive interaction with satellites or companions.

Marino et al. (2010) imaged three nearby galaxy groups (LGG 93, LGG 127, and LGG 225) in the far and near ultraviolet with the Galaxy Evolution Explorer. NGC 3501 and its companion NGC 3507 are members of LGG 225. They found for nine spiral galaxies in LGG 225 luminosity-weighted ages from a few to around 7 Gyr. They also found that LGG 225 is in a pre-virial collapse phase and still undergoing dynamical relaxation. This means that galaxies in LGG 255 are in a more active evolution phase than the other two groups. Moreover, the two galaxies NGC 3501 and NGC 3507 are about 12.6 arcmin (86 kpc) apart, show no signs of interaction in the optical (Knapen et al. 2014) but show signatures of distortion in the UV morphology (Marino et al. 2010). Comparing their masses, NGC 3507 has a stellar mass of about 1.3×10^{10} $M_{\odot}$ (Sheth et al. 2010) which is similar to the total stellar mass of NGC 3501 being around 1.5×10^{10} $M_{\odot}$ (Sheth et al. 2010).

Finally, Martín-Navarro et al. (2012) studied the surface brightness profile of NGC 3501 and found a first break at a radius of ∼67 arcsec (7.6 kpc) and a further truncation at ∼100 arcsec (11.36 kpc) from the centre. They propose that the inner break might be related to a threshold in the ongoing star formation and that the truncation is more likely a real drop in the stellar mass density of the disc associated with the maximum angular momentum of the stars.

With the use of integral-field spectroscopy and especially by mapping the stellar population and star formation history, we gain a more detailed view and can search for small differences in the disc structure.

3 OBSERVATIONS AND DATA REDUCTION

The data were obtained using MUSE (Bacon et al. 2010) at the Unit Telescope 4 of the Very Large Telescope, located in the Atacama Desert of northern Chile. MUSE is a panoramic integral-field spectrograph that has a field of view of 1 squared arcmin in Wide-Field Mode (WFM) and a spatial sampling of 0.2 squared arcsec. It can observe objects in a wavelength range of 4650–9300 Å and has a mean spectral resolution of $R = 3000$.

NGC 3501 was observed in Period 98, as part of the ESO program 098.B-0662 (PI: Pinna, F.), from 2016 December 30 to 2017 February 20. We used two MUSE-WFM pointings, an inner one that covers the central region of the galaxy, and an outer one towards the outer south-western part of the galaxy. The inner pointing was observed in one observing block with a total exposure time of 2200 s, while the outer pointing was observed in eight observing blocks with a total exposure time of 17 920 s. This results in a total exposure time of 20 120 s (∼5.6 h) for both pointings. The data were reduced as described in Gadotti et al. (2019), using the MUSE pipeline (version 1.6) from Weilbacher et al. (2012). The two single pointings were initially combined into a mosaic, but we found significant offsets right at the edges of the pointings in the stellar population parameters. These offsets could result from different sky subtraction in the two pointings, or perhaps from the particular way we build the mosaic. Investigating this issue is beyond the scope of this paper, as we found that these offsets were greatly minimized when working with the two cubes separately. The results presented here thus use measurements from the individual cubes. Since the bins of the outer pointing have a better spatial resolution than the bins of the inner pointing in the overlapping region, due to the higher signal-to-noise ratio (SNR) per pixel (because of the longer exposure time), we use the values from the outer pointing for the overlapping region.

4 ANALYSIS

4.1 Voronoi binning

The data cubes were binned, using the Voronoi binning method of Cappellari & Copin (2003). This method performs an adaptive spatial binning of integral-field spectroscopy data to reach a previously given

Downloaded from https://academic.oup.com/mnras/article/520/2/3066/7008533 by guest on 17 May 2023

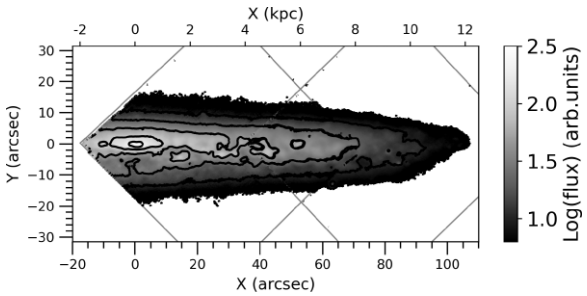

Figure 2. Flux map of NGC3501 obtained with the two MUSE pointings. The approximate positions of the MUSE pointings are indicated by grey lines, while the isophotes are displayed in black.

minimum SNR per bin. It preserves the maximum possible spatial resolution of our data, for a given minimum SNR.

The resulting data of the inner pointing consists of 217 Voronoi bins with a target SNR = 40 per bin, taking into account all spaxels. The outer pointing results in 130 Voronoi bins, also with a target SNR = 40, but including only spaxels with a minimum SNR of 2. The different SNR thresholds were chosen such that the Voronoi bins of the two pointings extend to a similar flux level, and a continuous and clean transition at the edges of the two pointings is ensured. In this step, the spectra of the bins were cut to the wavelength range of 4750–5500 Å, so most regions in which the sky subtraction could have left residuals (at longer wavelengths) were avoided. Also, the age sensitivity of the used stellar population models (see Section 4.2) weakens towards longer wavelengths, which also include features that are not sensitive to α-enhancement. Finally, the data were cut to a specific spatial range to avoid residual spaxels appearing outside of the galaxy. A flux map of NGC 3501 can be seen in Fig. 2.

Extending the wavelength range to around 7000 Å and including the Hα and [N II] emission lines is beyond the scope of this paper, and will be done in a future project.

4.2 Stellar population models

In this paper, we used MILES single-stellar population (SSP) models from Vazdekis et al. (2015), which are based on BaSTI isochrones, to fit the spectra of the Voronoi bins. All models have a spectral resolution of 2.51 Å (Falcón-Barroso et al. 2011), while covering the full wavelength range from 3540 to 7410 Å. Vazdekis et al. (2015) also give safe ranges[1] of SSP models for different spectral ranges and advise to use models with safe age and metallicity. Since we observed NGC 3501 in the optical and wanted to be in the safe range, we needed to exclude SSP models in metallicity and age. Therefore, we used models with 9 metallicity [M/H] values from −1.26 up to +0.40. Also, we used 28 age values going from 0.5 to 14 Gyr, evenly spaced every 0.5 Gyr, and two [α/Fe] $\approx$ [Mg/Fe] values: 0.0 dex (solar abundance) and 0.4 dex (supersolar abundance). This results in a total amount of 504 models.

4.3 Stellar kinematic fitting

For the fitting of the stellar kinematics, we used the PYTHON[2] version 7.4.2 of the full-spectrum penalized PiXel-Fitting (PPXF) method of Cappellari & Emsellem (2004) and Cappellari (2017). PPXF fits a combination of SSP models to the full stellar spectrum of the Voronoi bins, with a maximum penalized likelihood approach, to recover the line-of-sight velocity distribution (LOSVD). This is described as a Gauss-Hermite expansion and includes stellar mean velocity, velocity dispersion and higher moments. Since we observed that the galaxy has strong emission in Hβ (4861.33 Å;), [O III] (4958.92 & 5006.84 Å;), and [N I] (5197.90 & 5200.39 Å;), these spectral lines were masked with a masking window of 800 km s^{-1} and left out for the kinematic PPXF fitting. We applied additive polynomials of fourth degree and used the first four moments (V, σ, h_3, h_4) of the LOSVD for the fitting, which were obtained as output. Also, we needed to discard five bins from the kinematic maps, because some spectra were too noisy or showed strong emission from foreground objects.

4.4 Gas emission line fitting

For extracting the stellar populations, a spectrum cleaned from the gas emission lines is needed. This is important as we want to fit the absorption spectra of the galaxy without masking regions of important absorption lines like Hβ, the most age-sensitive feature in the analysed range. Therefore, we used the Gas and Absorption Line Fitting (GANDALF) method, described by Sarzi et al. (2006), which allows us to fit both the stellar spectrum and the emission lines simultaneously, to subtract the emission lines from the rest of the spectrum and get a cleaned spectrum. We used a customized version of the one implemented in the GIST pipeline (Bittner et al. 2019) and fit the emission lines mentioned in Section 4.3. The resulting maps of the ionized gas are presented and discussed in Appendix A.

4.5 Stellar population fitting

We used PPXF, now with a different setup described below, to extract the stellar populations of NGC 3501. The combination of SSP models used by PPXF, to fit the observed spectra, allows us to extract mass- and light-weighted stellar-population parameters. For the mass-weighted results, the SSP models were kept as they are, since they are already normalized to have the mass of 1 M$_\odot$, but to obtain light-weighted results the SSP models were normalized by their own mean flux.

Because this galaxy has a lot of gas and dust, we first fitted each Voronoi bin spectrum with PPXF for dust extinction. Then we corrected the spectra for that using the output from the PPXF extinction fit together with a Calzetti (2001) extinction curve. Additionally, we corrected all spectra for the extinction of the Milky Way following Emsellem et al. (2022), where they used a Cardelli, Clayton & Mathis (1989) extinction law and E(B-V) values from Schlafly & Finkbeiner (2011) to determine the stellar continuum extinction. After that, we fitted each spectrum for the stellar population parameters with PPXF again, using a multiplicative polynomial of eigth degree and no additive polynomials. We set up a regularization for the stellar population weights as suggested in Cappellari (2017). Here, we used the calibration method explained e.g. in Boecker et al. (2020), to find the maximum allowed regularization parameter consistent with the data. With that method, we found that a wide range of values could be applied to the data. We then chose our regularization, in that range but much lower than the maximum value obtained from the calibration, following the approach described in Pinna et al. (2019a). We applied several values of regularization and examined the resulting fits. Moreover, we plotted the star formation history with different regularizations, to see if any features of age, metallicity and [Mg/Fe]-abundance will be lost with a higher value. In the end, a value of 10 was chosen, as a good compromise between smoothing

[1] http://research.iac.es/proyecto/miles/pages/ssp-models/safe-ranges.php
[2] www.python.org

Downloaded from https://academic.oup.com/mnras/article/520/2/3066/7008533 by guest on 17 May 2023

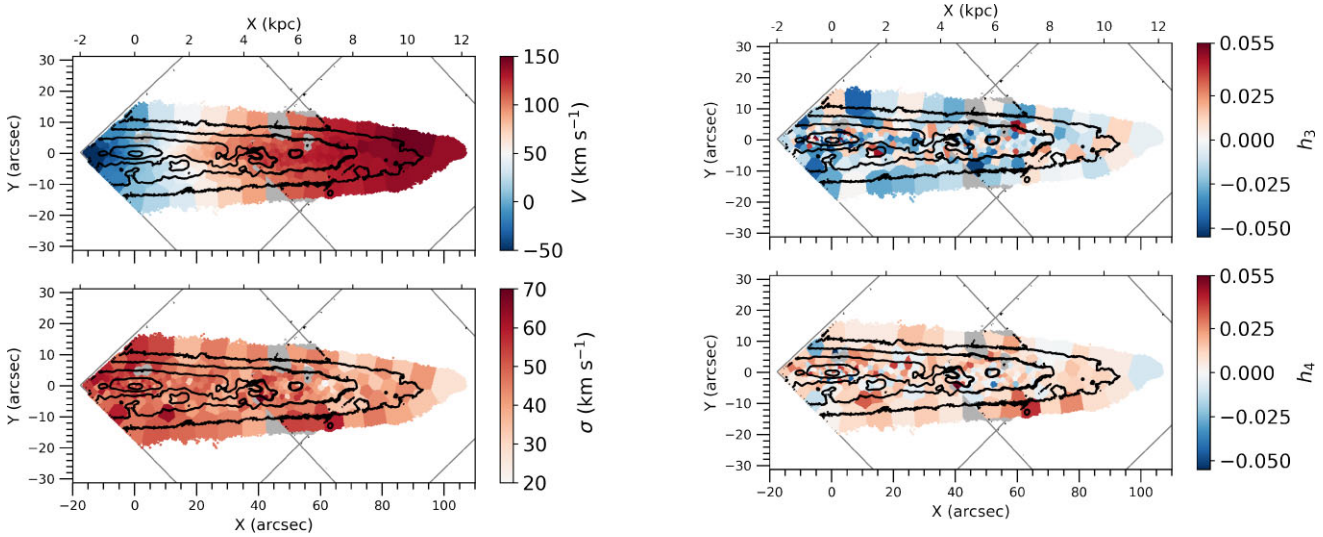

Figure 3. Left: Stellar kinematic maps of the mean velocity V (upper panel) and velocity dispersion σ (bottom panel) of the stellar LOSVD. Right: Kinematic maps show values of h_3 and h_4 as results from the stellar kinematic PPXF fitting. The discarded bins are plotted in grey and the approximate positions of the MUSE pointings are indicated by grey lines, while the isophotes are displayed in black.

the results but still being able to identify clearly different features in the age, metallicity and [Mg/Fe] distributions.

After examining the final fits, we discarded nine more bins because of ill GandALF or stellar population fitting. In the end, we are left with a total number of 305 Voronoi bins in both pointings that provided good fits in each step.

4.6 Uncertainties in stellar kinematic and population fitting

We performed Monte Carlo simulations to estimate the uncertainties. Therefore, we first fitted the spectra of each Voronoi bin with PPXF using the setup described in Section 4.5 and calculated the wavelength-dependent residuals as the difference between the best-fitting spectrum from PPXF and the initial galaxy spectrum. We then added noise to the initial spectra, where for each spectral pixel the noise is taken from a Gaussian distribution of standard deviation equal to the residuals. We obtained the uncertainties in all kinematic and stellar population analysis by computing the standard deviation of a thousand realizations of the input spectra. Typical values for the uncertainties of V, σ, h_3, and h_4, respectively, are: $\sim 10\,\mathrm{km\,s^{-1}}$, $20\,\mathrm{km\,s^{-1}}$, 0.02, and 0.01. The uncertainties for the light-weighted (mass-weighted) results for age, metallicity [M/H] and [Mg/Fe] respectively are: $\sim$ 1 (2) Gyr, 0.1 (0.15) dex, 0.05 (0.1) dex. For more details, the uncertainty maps of the stellar kinematics and stellar population parameters are shown in Figs B1 and B2.

5 RESULTS

We start this section by describing stellar kinematics and population maps. The two single pointings were aligned using the isophotes, which are plotted in black. All the discarded bins are plotted in grey and the approximate positions of the MUSE pointings are indicated by grey lines.

5.1 Stellar kinematics

The stellar kinematic maps of the mean velocity V, velocity dispersion σ, h_3 (skewness), and h_4 (kurtosis) are presented in Fig. 3.

In the velocity map (left upper panel in Fig. 3), a smooth rise of the velocity going from the centre outwards of the galaxy, with a maximum rotation velocity of $\sim$150 km s^{-1} can be seen. Within the uncertainties, this maximum rotation velocity is in good agreement with the circular velocity from Sheth et al. (2010) seen in Table 1. Lines with the same velocity are vertical in the centre of the galaxy and get more V-shaped in the outer parts indicating a faster rotation of the mid-plane in comparison to regions at larger heights. In the map of the velocity dispersion (left bottom panel in Fig. 3), we clearly see a radial gradient, from higher values in the centre to lower values in the outer regions, with a slight rise at around 40 arcsec. A vertical gradient could not be observed.

The map of the Gauss–Hermite parameter h_3 (top right map in Fig. 3), which describes how much the LOSVD deviates from a symmetrical Gaussian (Gerhard 1993; van der Marel & Franx 1993), shows overall negative values of h_3. Some positive values of h_3 can be seen in the mid-plane at the centre of the galaxy. An anticorrelation with the mean velocity is usually associated with different rotating components of the galaxy (e.g. Krajnović et al. 2008; Pinna et al. 2019b). However, because higher moments are penalized by PPXF when the SNR is low (Cappellari & Emsellem 2004), we find very low values for h_3 and no components like a thin disc can be clearly identified here. In the map of the Gauss–Hermite parameter h_4 (right bottom map in Fig. 3), characterizing the heaviness of the LOSVD tails compared to pure Gaussian tails (Gerhard 1993; van der Marel & Franx 1993), one can see mostly positive values (broader profiles than a Gaussian) and some negative values across the mid-plane (narrower profiles than a Gaussian). With that, no structures can be clearly identified here either.

5.2 Stellar population

The maps of the light-weighted (left-hand panels) and mass-weighted (right-hand panels) stellar populations are presented in Fig. 4. Because every SSP model matches a combination of age, metallicity [M/H], and [Mg/Fe]-abundance, the weights given to them by PPXF indicate how important each combination is for every individual bin. Therefore, each bin shows a weighted average of the stellar

Downloaded from https://academic.oup.com/mnras/article/520/2/3066/7008533 by guest on 17 May 2023

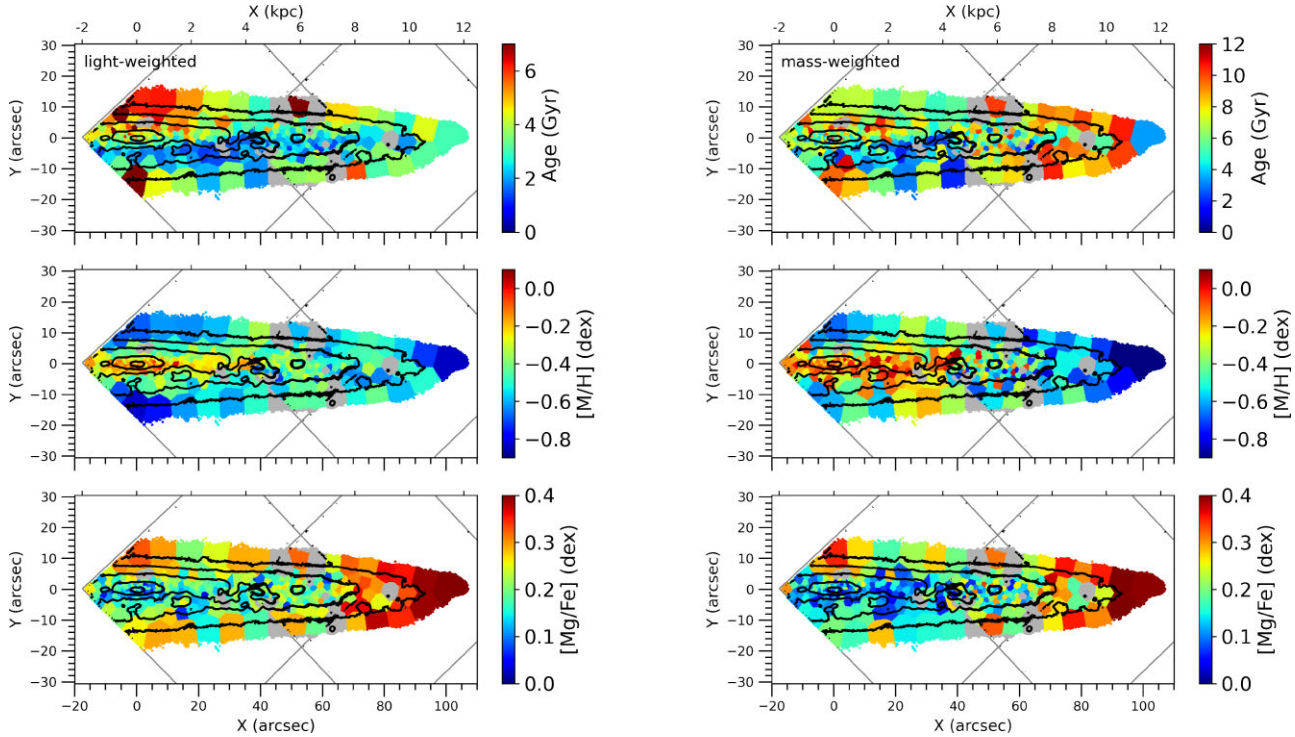

Figure 4. Left: Stellar population maps showing the light-weighted age (top), total metallicity [M/H] (middle), and [Mg/Fe]-abundance (bottom). Right: Stellar population maps showing the mass-weighted age (top), total metallicity [M/H] (middle), and [Mg/Fe]-abundance (bottom). The approximate positions of the MUSE pointings are indicated by grey lines and the discarded bins are displayed in grey, while the isophotes are displayed in black.

population parameters. In the maps, mass- and light-weighted age, metallicity [M/H], and [Mg/Fe]-abundance are displayed.

In the age maps (top maps in Fig. 4), we see a horizontal stripe of very young stars directly below the central mid-plane. This stripe extends for 0 arcsec < X < 40 arcsec in the mass-weighed map and up to 70 arcsec in the light-weighted map. The weight of younger stars is enhanced in light-weighted results, since they are more dominant in light compared to older stars. On the other hand, older stars are more dominant in mass, so they appear more pronounced in mass-weighted results. This is also the reason why the light-weighted map shows on average younger stars than the mass-weighted map in the whole galaxy (also seen in e.g. Sánchez-Blázquez et al. 2014). As seen in Fig. 1, dust is visible close to the mid-plane, blocking some of the light from stars in this region. So here the light of stars which are closer in the line of sight and tend to be younger is also integrated. However, larger gaps in the dust, that can be seen in the SDSS image of NGC 3501 in Fig. 1, ensure that most of the light integrated along the line of sight has its origin in the galaxy mid-plane region laying behind the dust. The rest of the galaxy shows a mixture of mostly intermediate-age stars and some very old stars with ages going up to 12 Gyr in the mass-weighted map. We can identify the very young stars in the mid-plane of the light-weighted age map as an inner thinner disc-like structure embedded in the older, extended and thicker disc. This difference is less clearly seen in the mass-weighted map.

Looking at the metallicity [M/H] maps (middle maps in Fig. 4), the highest metallicity can be found in the inner mid-plane of the galaxy (with some regions reaching a solar metallicity), surrounded by lower metallicity values in the outer and thicker disc. In the mid-plane, some spots with solar metallicity are visible. This negative vertical gradient is stronger in the light-weighted results than in the mass-weighted ones, but is clearly visible in both maps and also in both MUSE pointings. The mass-weighted map also shows a negative radial gradient in metallicity. In the light-weighted metallicity map, this gradient is not so pronounced. Comparing the light-weighted and mass-weighted metallicities, the stars in the mass-weighted maps are more metal-rich than the ones in the light-weighted maps, especially those in the mid-plane and the centre of the galaxy. Furthermore, the mass-weighted metallicity map had overall higher values than the light-weighted map and with Monte Carlo simulations, we obtained on average slightly larger uncertainties for mass-weighted ages, metallicities, and [Mg/Fe]-abundances. For more details, maps of the uncertainties are shown in Fig. B2.

The maps of the [Mg/Fe]-abundance (bottom maps in Fig. 4) show a clear anticorrelation with the metallicity maps. The highest supersolar [Mg/Fe] values are located in the outer regions. The lowest [Mg/Fe]-abundance can be found in the centre of the galaxy, best visible as a small blueish stripe in the centre of the light-weighted map. In the mass-weighted one, this region with low [Mg/Fe] values extends further to the outer regions, but is still more dominant in the central mid-plane, reaching partially solar abundances. Positive vertical and radial gradients are visible in both maps, whereas the radial gradient is more pronounced in the mass-weighted abundances. The inner and thinner disc-like structure of very young stars in the mid-plane appears to be also the most metal-rich and least [Mg/Fe] enhanced, embedded in the older, metal-poor and [Mg/Fe]-enhanced thicker disc structure.

5.3 Star formation history

Because of the differences in age, metallicity [M/H], and [Mg/Fe] between different regions of the galaxy, described in Section 5.2, we define two components: metal-rich and metal-poor. This separation is based on the large jumps in the vertical and radial metallicity and

Downloaded from https://academic.oup.com/mnras/article/520/2/3066/7008533 by guest on 17 May 2023

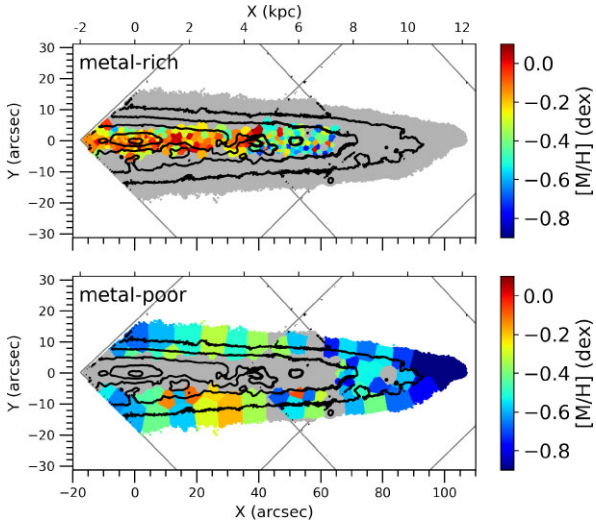

Figure 5. Mass-weighted metallicity maps, where the metal-rich (top) and metal-poor (bottom) components are indicated. In each panel, all the bins of the other component are plotted in grey and the approximate positions of the MUSE pointings are indicated by grey lines, while the isophotes are displayed in black.

[Mg/Fe] abundance. The highest metallicity and lowest [Mg/Fe] bins are therefore included in the metal-rich component, while the lower metallicity and higher [Mg/Fe] bins are included in the metal-poor component. Those components are visualized in Fig. 5, using the mass-weighted metallicity map (Fig. 4, right).

To get the star formation history of each component normalized by the total stellar mass of the covered galaxy half, we calculated the mass of each Voronoi bin as described in Pinna et al. (2019a). For that, we used an SDSS g-band image of NGC 3501 from DR16 (Ahumada et al. 2020), as well as the mass-to-light ratios in each Voronoi bin calculated by combining our mass-weighted results with the corresponding mass-to-light ratios to our models from Vazdekis et al. (2015). For the region that is covered by our Voronoi bins, we derived a total stellar mass of 5×10^9 $M_\odot$. This value is compatible with the total stellar mass in Table 1, calculated in the 3.6 and 4.5 μm bands, by also taking into account that half of the galaxy mass is missing in our two MUSE pointings and a significant amount of stellar light in the optical range may be obscured by the dust. Moreover, the metal-rich component covers 28 per cent of the Voronoi binned region, making up 1.4×10^9 $M_\odot$, whereas the metal-poor component covers 72 per cent, making up 3.6×10^9 $M_\odot$.

The resulting star formation history is plotted in Fig. 6, in terms of the mass fraction of the covered galaxy as a function of age. The age bins are colour-coded by the weighted-average metallicity [M/H] (left) and the weighted-average [Mg/Fe] (right). Those values were derived as the average metallicity [M/H] or [Mg/Fe] for each age bin in the component, weighted by their respective mass fractions. The star formation history of the metal-rich component is plotted at the top, whereas the star formation history of the metal-poor component is plotted at the bottom.

Looking only at the slope of the star formation history, the metal-rich and metal-poor components peak for old ages around 14 Gyr. Later on, the star formation slightly decreases but does not stagnate and peaks again at youngest ages in both components. So the metal-rich component forms steadily. For the metal-poor component, we also see a peak around 8 Gyr, so different bursts of star formation are visible here.

Uncertainties for the mass fractions indicated in these star formation histories are ∼0.003 (0.015) for the metal-rich (metal-poor) component. The detailed uncertainties, computed from Monte Carlo simulations, are shown in Appendix B.

5.4 Chemical evolution

If we look at the colour-coded bars (Fig. 6), we see for both components subsolar metallicities at all ages. On average, the metal-rich component has by definition an overall higher metallicity (from −0.1 to −0.4 dex) and an overall lower [Mg/Fe] than the metal-poor component (from 0.1 to 0.2 dex). By contrast, the metal-poor component has a more extended metallicity range (from around −0.1 to −0.8 dex) and its [Mg/Fe] reaches higher values (from around 0.2 to 0.3 dex).

Starting with the metal-rich component (top), we see that stars formed in the peak at 14 Gyr do not show the lowest metallicity nor the highest [Mg/Fe]. The metallicity then slightly decreases and stays relatively steady till ∼5 Gyr. After that, the metallicity increases to nearly solar values, while the star formation history reaches its second big peak at the latest ages. During that, the [Mg/Fe] oscillates slightly until 0.5 Gyr, where it increases to higher abundances. Continuing with the metal-poor component (bottom), we see at the oldest ages a higher mass fraction with a lower metallicity and higher [Mg/Fe] compared to the metal-rich component. Younger populations at around 12 Gyr then have a significantly lower metallicity. From 12 Gyr on, towards the youngest ages, we observe oscillations in metallicity, following a chemical enrichment that alternates with metallicity drops. In this metal-poor component, [Mg/Fe] also oscillates as anticorrelated to metallicity, where higher [Mg/Fe]-abundances correspond to peaks in star formation as well as to drops in metallicity. The highest [Mg/Fe]-peak then appears at the youngest ages.

So while the inner mid-plane evolves rather slowly and evenly with a more balanced [Mg/Fe] ratio, the more extended and thicker metal-poor component suffered from several bursts leading to the formation of more metal-poor and [Mg/Fe]-enhanced stars. Uncertainties for the metallicity [M/H] and [Mg/Fe] values indicated in these star formation histories are for the metal-rich (metal-poor) component: ∼0.15 (0.3) dex in [M/H] and ∼0.05 (0.1) dex in [Mg/Fe]. The detailed uncertainties, computed from Monte Carlo simulations, are shown in Appendix B. The youngest bins with high [Mg/Fe] abundance are marked with dashed edges to warn the reader about the low reliability of those values. This and other aspects are extensively discussed in Appendix C.

6 DISCUSSION

In spite of the potential large systematic uncertainties for the youngest stars, and being aware of the limitations of our method (all discussed in Appendix C), we strongly support the oscillations in [Mg/Fe] and metallicity for older ages in the star formation histories (Fig. 6). These are discussed in the following sections.

6.1 Disc structure

Our kinematic maps (Fig. 3) do not show two clearly distinct disc structures, in agreement with the morphological decomposition from Comerón et al. (2018), who suggested that NGC 3501 consists of a single thicker stellar disc. A sharp vertical jump in velocity dispersion would imply a two-disc structure for the galaxy, as it is observed in other edge-on galaxies (e.g. Pinna et al. 2019a, b) that have distinct

Downloaded from https://academic.oup.com/mnras/article/520/2/3066/7008533 by guest on 17 May 2023

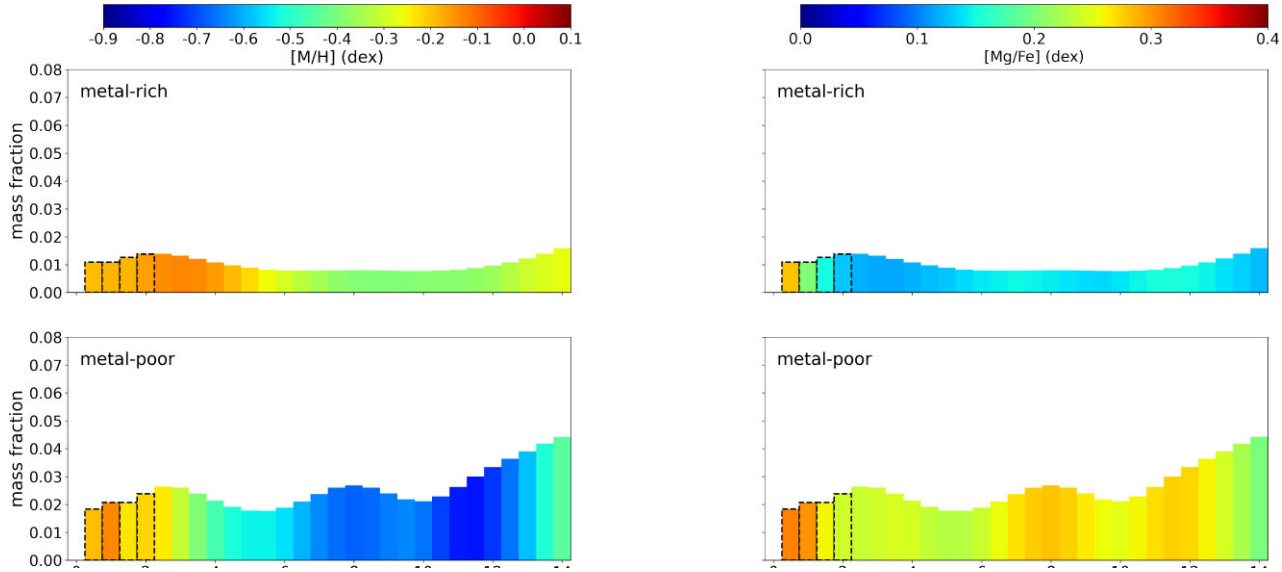

Figure 6. Star formation history in terms of the mean mass fraction (normalized to the galaxy mass in the region covered by our data) in the metal-poor (bottom) and metal-rich (top) components as a function of age. Age bins are colour-coded by metallicity [M/H] (left), and by [Mg/Fe] (right). Black dashed edges mark age bins with [Mg/Fe] abundances that we do not consider totally reliable, because of difficulties in retrieving the [α/Fe] for young stars as discussed in Appendix C.

thick and thin discs, where the velocity dispersion is higher in the thick disc than in the thin disc. The rise in velocity dispersion at around 40 arcsec might be the result of turbulent star formation in a spiral arm structure of the galaxy. This star formation region is also visible in Fig. A1, where one can see the high flux of H β and [O III] emission lines in this specific region of higher stellar velocity dispersion, which also has a higher velocity dispersion in the gas component, as it can be seen in Fig. A2.

Because the galaxy is not seen completely edge-on, some part of the boxy bulge is visible at the top centre of the galaxy with a higher velocity dispersion. However, the bulge is faint and we do not see a box-shaped pattern of high values in velocity dispersion in the bulge region (as it was found e.g. in Pinna et al. 2019a). So the box-shape from Lütticke et al. (2000) could not be observed in our kinematic maps. We cannot provide more details on the bulge since it cannot be identified either in any of the stellar population maps.

We know that most galaxies displaying a thin and thick disc show concrete differences in their vertical age distribution, where the thin disc shows an overall younger population than the thick disc (e.g. Yoachim & Dalcanton 2008b; Kasparova et al. 2016; Martig et al. 2021; Scott et al. 2021). In contrast to early-type galaxy observations, we see ongoing star formation in NGC 3501, so stellar populations of this galaxy are rather young and uniform (Fig. 4). This is also in good agreement with the ages derived in Marino et al. (2010) (see Section 2) and their findings that NGC 3501 is in an unvirialized phase, which could be the reason for active star formation.

The metallicity distribution of mass- and light-weighted results (Fig. 4) shows negative gradients from average solar and slightly subsolar metallicities for the stars in the inner mid-plane to subsolar metallicities and lowest values in the outer envelope of the galaxy. While the [Mg/Fe] distribution showed positive gradients from nearly solar values in the mid-plane to supersolar values in the outer galaxy parts.

The negative radial metallicity gradient is also seen by Márquez et al. (2002) for this galaxy (see Section 2). Sharp vertical gradients can be seen in Comerón et al. (2016), Guérou et al. (2016, only metallicity), and Pinna et al. (2019a, b, metallicity and [Mg/Fe]) for their analysed S0 galaxies, where high supersolar metallicities and nearly solar [Mg/Fe] abundances are found in the mid-plane and lower metallicities and supersolar [Mg/Fe] in the thick disc. The differences in metallicity are more prominent in Pinna et al. (2019a,b) and NGC 3501 than in Comerón et al. (2016) and Guérou et al. (2016). The overall anticorrelation of [Mg/Fe] to metallicity that we see in the maps and the star formation history was observed too in other external galaxies and in the Milky Way (e.g. Pinna et al. 2019a, b; Bittner et al. 2020; Wheeler et al. 2020). Although S0 and Sc galaxies have different morphologies and had different evolution histories, the differences in S0 metallicities associated with the presence of a thick and a thin disc, help us to associate the differences in our metallicity maps to different disc components, with probably different origins. Also, the Milky Way shows negative metallicity and positive [α/Fe] gradients, where more solar metallicities and [α/Fe] abundances are located in the mid-plane and subsolar metallicities and slightly supersolar [α/Fe] values in the thicker disc at larger distances from the mid-plane (Minchev et al. 2019; Wheeler et al. 2020; Gaia Collaboration 2022), while having some flaring of the thin disc at larger radii. This metallicity and [α/Fe] gradients in the Milky Way were associated with an 'inside-out' scenario, where the more metal-rich and α-poor thin disc formed from the inside-out embedded in a more metal-poor and α-rich thick disc (e.g. Minchev, Chiappini & Martig 2013; Schönrich & McMillan 2017; Frankel et al. 2019; Gaia Collaboration 2022). Moreover, Scott et al. (2021) found α-rich and α-poor stellar populations in the Milky Way-like galaxy UGC 10738, that have a similar spatial distribution to the Milky Ways α-rich and α-poor populations.

One can also see from Fig. 5 that our metal-rich component, which extends to around 65 arcsec, agrees very well with the first break radius from Martín-Navarro et al. (2012) at ∼67 arcsec (see Section 2), related to a threshold in ongoing star formation. This threshold can be seen in the distribution of younger stars in the metal-rich component, whereas the metal-poor component consists of older

Downloaded from https://academic.oup.com/mnras/article/520/2/3066/7008533 by guest on 17 May 2023

stars on average. The truncation radius at ∼100 arcsec (Martín-Navarro et al. 2012), which is rather a real drop in the stellar mass density of the disc, lies near the limit of our Voronoi binning at around 108 arcsec. Here, the Voronoi binning ends because of the given SNR-threshold for the spaxels. The SNR is lower for lower luminosity regions, caused by the lower stellar mass density in the outer regions of the galaxy.

So stars with younger ages, higher metallicities and lower [Mg/Fe]-abundances in the inner mid-plane, embedded within older stars, with subsolar metallicities and supersolar [Mg/Fe]-abundances, suggest that two disc components are present. Moreover, in the mid-infrared image of NGC 3501 from Comerón et al. (2018), less affected by the dust in the galaxy than our MUSE data in the optical range, a thin and much brighter structure is visible in the inner mid-plane. However, Comerón et al. (2018), aiming at fitting vertical profiles in different radial bins to identify different disc components, excluded this central region which extends between −25 and 25 arcsec in the radial direction, because it may be contaminated by the bulge. That brighter inner region spatially matches the young age, high-metallicity and low-[Mg/Fe]-abundance structure in the central mid-plane, seen on our stellar population maps (Fig. 4). So we propose the presence of two structural disc components in that radial range: a thicker metal-poor and older main component, with a much less radially extended metal-rich thin disc, recently formed.

6.2 Formation and evolution of NGC 3501

In the following, we will place the results of the stellar kinematics, population, and star formation history analysis of NGC 3501 in context with its formation history.

In the star formation history (Fig. 6) of the metal-poor component (bottom panels), we see higher metallicities at very old ages with a significant drop later around 12 Gyr ago. This drop is also seen in the metal-rich component, but less enhanced. Such relatively high metallicities at early times are also seen in closed-box chemical evolution models by Vazdekis et al. (1996), where high metallicities can be achieved very quickly with very intense star formation. Another possibility to produce higher metallicities at old ages is to accrete metal-rich old stars during the evolution process of the galaxy (Feuillet et al. 2022).

To explain the drop in metallicity around 12 Gyr ago, associated with an increase of [Mg/Fe], we propose the accretion of a large mass of pristine gas from the outside, followed by a burst of star formation from that external gas. A second burst of star formation from more pristine gas explains as well the more metal-poor and [Mg/Fe]-enhanced peak in the star formation history of the metal-poor component about 8 Gyr ago. So the bursts in the metal-poor component correspond to different episodes of gas accretion. Our interpretation of these oscillations in metallicity and [Mg/Fe] is the combination of the internal chemical enrichment, similar to what we would have in a closed-box, and the contribution of bursts of star formation from external material. The metal-rich component is not very affected by those bursts and seems to keep forming stars at the same pace. So in general, the external parts of the galaxy might be more affected by accretion.

Márquez et al. (2002) suggested that NGC 3501 and the nearby face-on galaxy NGC 3507 may be mildly interacting, using the region of Hα emission. No signs of this mild interaction were found in the optical using SDSS by Knapen et al. (2014) though. These interactions between NGC 3501 and other galaxies in LGG 225 could drive the pristine gas into NGC 3501 and enhance the star formation events. The drop in metallicity could then come from metal-poor gas inflow along filaments or even from the interactions with surrounding galaxies.

The youngest starburst is observed to be the most metal-rich and α-enhanced. This starburst might also explain the higher [Mg/Fe] values in the light-weighted maps, compared to the mass-weighted maps, since the former are more biased towards younger stars than the latter (see also Section 5.2). Usually, [Mg/Fe] increases with age (e.g. Rahimi et al. 2011; Nissen 2015) and would rather be lower than higher for younger stars. Also, most of the results from Bittner et al. (2020) show equal [α/Fe]-abundances for mass- and light-weighted results. Only a few galaxies from their sample show lower [α/Fe]-abundances in the mass-weighted maps, which the authors explained with higher uncertainties in their mass-weighted [α/Fe] maps. This young population of higher [Mg/Fe] and metallicity here, could rather be the result of a sudden and significant increase in the star formation efficiency (Conroy et al. 2022).

As seen in Section 5.3 for NGC 3501, the stellar mass of the thicker metal-poor component is currently much larger than the one of the thinner metal-rich component. Comerón et al. (2011) show that the thin disc typically is the more dominant stellar mass component for galaxies with a circular velocity of around 150 km s^{-1}. However, a comparison with this trend from Comerón et al. (2011) is complicated, since NGC 3501 is atypical. The thinner metal-rich component of NGC 3501 has not fully formed yet and the metal-rich and metal-poor components of NGC 3501 are not comparable to typical thin and thick discs (e.g. in scale height, velocity dispersion, mass). Also, if we extrapolate the trends of the star formation history in Fig. 6, the thicker metal-poor component seems to keep forming stars at a similar pace as the thinner metal-rich component. Since this region of higher metallicity will likely grow into the parts of the galaxy that are more metal-poor now and we currently do not know how far the metal-rich region will expand until it becomes a more typical thin disc, it is difficult to measure the star formation rate belonging to a future thin disc and give a secure estimate on the mass evolution of the metal-rich component right now.

It is important to mention that the thicker, metal-poor disc is also present in the inner mid-plane, overlapping in the line of sight to the metal-rich component. This could bias the inner metal-rich region towards lower metallicities, higher [Mg/Fe] and older stars on average, contributing some features of the metal-poor component (lower metallicity in intermediate ages, higher [Mg/Fe] around 8 and 12 Gyr, higher fraction of stellar mass around 14 Gyr in age) in the star formation history of the metal-rich one. We checked for contamination of the thicker metal-poor disc in the metal-rich component in radial direction by restricting the metal-rich component only to around 40 arcsec. We found that the continuous star formation in the metal-rich component, as well as values for metallicity and [Mg/Fe] do not change in a relevant amount.

Altogether, older ages, low metallicities, and the [Mg/Fe] enhancement suggest that the thicker more-extended region of the galaxy formed faster. By contrast, the younger metal-rich inner mid-plane in NGC 3501 kept evolving from subsolar to solar metallicities and a more balanced [Mg/Fe]-abundance. In terms of galaxy evolution, Yu et al. (2021) showed that each galaxy has a bursty period of star formation in early times, leading into a steady phase having a nearly constant star formation rate. Stars in the bursty phase are mostly scattered into hot orbits, not being arranged in a thin disc yet. This bursty phase then ends and the steady phase begins, where a thin disc becomes more pronounced. Similarly, in the 'born-hot' scenario (Brook et al. 2004), the thick disc forms *in situ* at high redshift and the

Downloaded from https://academic.oup.com/mnras/article/520/2/3066/7008533 by guest on 17 May 2023

thin disc forms from gas accretion during multiple mergers. The stars forming in the bursty phase are today found in a thick disc structure, whereas young stars in the steady phase are located in a thin disc. This scenario could explain the more bursty star formation history of NGC 3501s metal-poor component, while also leading to a more steady star formation history of the metal-rich component. A positive radial [Mg/Fe] gradient might be a feature of galaxies formed through an 'outside-in' formation scenario, because the outer disc develops earlier and faster than the inner region, probably leaving outer radii in higher [Mg/Fe]-abundances (shown for elliptical galaxies in Pipino & Matteucci 2004; Pipino, Matteucci & Chiappini 2006 and low-mass galaxies in e.g. Gallart et al. 2008; Zhang et al. 2012). NGC 3501 also shows positive vertical and radial [Mg/Fe] gradients, supporting this scenario. Also, the star formation history suggests that the extended component was already born as a thicker disc during a bursty period, and was undergoing several bursts of star formation. By contrast, the inner mid-plane evolved more steadily and might be less affected by incoming material from the outside than the outer envelope. While the full galaxy may be following an 'outside-in' formation since the outer metal-poor component was formed first, and only later the inner metal-rich disc, the latter may be the early innermost region of a future extended thinner disc, forming 'inside-out'.

7 CONCLUSION

Two-dimensional maps of the stellar kinematics and populations as well as the star formation history of the late-type galaxy NGC 3501 have been obtained, using deep MUSE integral-field spectroscopy. Two MUSE pointings were used to observe the south-western half of the galaxy, which is seen edge-on. Maps of the mean velocity and velocity dispersion support a single disc-like rotation with a slightly faster rotation of the mid-plane region. We were able to see higher velocity dispersion at the centre of the galaxy, which may coincide with the central boxy bulge of the galaxy (Lütticke et al. 2000). Maps of the mass- and light-weighted stellar age, metallicity [M/H], and [Mg/Fe]-abundance were presented. These maps showed that the galaxy consists mostly of young stars with a positive vertical and radial gradient in age, clearer in the light-weighted maps. The metallicity maps show solar values in the inner mid-plane, with a vertical and radial gradient to subsolar metallicities in the outer envelope. The [Mg/Fe] abundance showed solar values in the inner mid-plane and supersolar abundances at larger radii and heights. Those gradients and the different star formation histories indicate a small thin disc existent in NGC 3501.

During the first stages of the evolution of NGC 3501, there was a single thicker disc probably born already thick in a bursty phase, with global lower metallicity and more significant [Mg/Fe] enhancement than components formed later. On the other hand, in the inner mid-plane, a thin disc-like structure slowly developed in a more steady phase, leading to solar metallicities and a lower [Mg/Fe]-abundance in the later phases of its evolution. Since NGC 3501 is gas-rich and mildly interacting, external events might have brought more-pristine gas with lower metallicities and more enhanced in α-elements, leaving several more [Mg/Fe]-enhanced populations formed from this external material in the outer parts of the galaxy. Because of its young age, NGC 3501 might be a galaxy in an early stage of galaxy evolution, showing a snapshot of the early evolutionary phase of a thin disc embedded in a thick disc. This galaxy will very likely form a more pronounced massive thin disc in the future, where the current central mid-plane already builds a base.

ACKNOWLEDGEMENTS

This work was funded by the Deutsche Forschungsgemeinschaft (DFG, German Research Foundation) – Project-ID 138713538 – SFB 881 ('The Milky Way System', subproject B08). FP and JF-B acknowledge support through the RAVET project by the grant PID2019-107427GB-C32 from the Spanish Ministry of Science, Innovation and Universities (MCIU), and through the IAC project TRACES which is partially supported through the state budget and the regional budget of the Consejería de Economía, Industria, Comercio y Conocimiento of the Canary Islands Autonomous Community. GvdV acknowledges funding from the European Research Council (ERC) under the European Union's Horizon 2020 research and innovation program under grant agreement No 724857 (Consolidator Grant ArcheoDyn).

DATA AVAILABILITY

The data described in this article are available on the ESO Science Archive Facility in the program 098.B-0662, PI: Pinna, F.

REFERENCES

Abadi M. G., Navarro J. F., Steinmetz M., Eke V. R., 2003, ApJ, 597, 21
Ahumada R. et al., 2020, ApJS, 249, 3
Ann H. B., Seo M., Ha D. K., 2015, ApJS, 217, 27
Bacon R. et al., 2010, in McLean I. S., Ramsay S. K., Takami H.eds, Proc. SPIE Conf. Ser. Vol. 7735, Ground-Based and Airborne Instrumentation for Astronomy III. SPIE, Bellingham, p. 773508
Baldwin C., McDermid R. M., Kuntschner H., Maraston C., Conroy C., 2018, MNRAS, 473, 4698
Bittner A. et al., 2019, A&A, 628, A117
Bittner A. et al., 2020, A&A, 643, A65
Boecker A., Leaman R., van de Ven G., Norris M. A., Mackereth J. T., Crain R. A., 2020, MNRAS, 491, 823
Bournaud F., Elmegreen B. G., Martig M., 2009, ApJ, 707, L1
Brook C. B., Kawata D., Gibson B. K., Freeman K. C., 2004, ApJ, 612, 894
Burstein D., 1979, ApJ, 234, 829
Calzetti D., 2001, PASP, 113, 1449
Cappellari M., 2017, MNRAS, 466, 798
Cappellari M., Copin Y., 2003, MNRAS, 342, 345
Cappellari M., Emsellem E., 2004, PASP, 116, 138
Cardelli J. A., Clayton G. C., Mathis J. S., 1989, ApJ, 345, 245
Casagrande L. et al., 2016, MNRAS, 455, 987
Cheng J. Y. et al., 2012, ApJ, 746, 149
Comerón S. et al., 2011, ApJ, 741, 28
Comerón S., Salo H., Janz J., Laurikainen E., Yoachim P., 2015, A&A, 584, A34
Comerón S., Salo H., Peletier R. F., Mentz J., 2016, A&A, 593, L6
Comerón S., Salo H., Knapen J. H., 2018, A&A, 610, A5
Comerón S., Salo H., Knapen J. H., Peletier R. F., 2019, A&A, 623, A89
Conroy C., Graves G. J., van Dokkum P. G., 2014, ApJ,780, 33
Conroy C. et al., 2022, arXiv e-prints (arXiv:2204.02989)
de Vaucouleurs G., de Vaucouleurs A., Corwin H. G. J., Buta R. J., Paturel G., Fouque P., 1991, Springer New York, NY Third Reference Catalogue of Bright Galaxies
Du W., Wu H., Zhu Y., Zheng W., Filippenko A. V., 2017, ApJ, 837, 152
Emsellem E. et al., 2022, A&A, 659, A191
Falcón-Barroso J., Sánchez-Blázquez P., Vazdekis A., Ricciardelli E., Cardiel N., Cenarro A. J., Gorgas J., Peletier R. F., 2011, A&A, 532, A95
Feuillet D. K., Feltzing S., Sahlholdt C., Bensby T., 2022, ApJ, 934, 21
Frankel N., Sanders J., Rix H.-W., Ting Y.-S., Ness M., 2019, ApJ, 884, 99
Gadotti D. A. et al., 2019, MNRAS, 482, 506
Gaia Collaboration, 2022, arXiv e-prints (arXiv:2206.05534)
Gallart C., Stetson P. B., Meschin I. P., Pont F., Hardy E., 2008, ApJ, 682, L89

Downloaded from https://academic.oup.com/mnras/article/520/2/3066/7008533 by guest on 17 May 2023

Gallart C., Bernard E. J., Brook C. B., Ruiz-Lara T., Cassisi S., Hill V., Monelli M., 2019, Nat. Astron., 3, 932
Ge J., Yan R., Cappellari M., Mao S., Li H., Lu Y., 2018, MNRAS, 478, 2633
Gerhard O. E., 1993, MNRAS, 265, 213
Gilmore G., Reid N., 1983, MNRAS, 202, 1025
Gilmore G., Wyse R. F. G., 1985, AJ, 90, 2015
Guérou A., Emsellem E., Krajnović D., McDermid R. M., Contini T., Weilbacher P. M., 2016, A&A, 591, A143
Hayden M. R., Recio-Blanco A., de Laverny P., Mikolaitis S., Worley C. C., 2017, A&A, 608, L1
Haynes M. P. et al., 2018, ApJ, 861, 49
Ivezić Ž. et al., 2008, ApJ, 684, 287
Jurić M. et al., 2008, ApJ, 673, 864
Kasparova A. V., Katkov I. Y., Chilingarian I. V., Silchenko O. K., Moiseev A. V., Borisov S. B., 2016, MNRAS, 460, L89
Kasparova A. V., Katkov I. Y., Chilingarian I. V., 2020, MNRAS, 493, 5464
Katkov I. Y., Kniazev A. Y., Kasparova A. V., Sil'chenko O. K., 2019, MNRAS, 483, 2413
Knapen J. H., Erroz-Ferrer S., Roa J., Bakos J., Cisternas M., Leaman R., Szymanek N., 2014, A&A, 569, A91
Koleva M., Prugniel P., Ocvirk P., Le Borgne D., Soubiran C., 2008, MNRAS, 385, 1998
Krajnović D. et al., 2008, MNRAS, 390, 93
Lütticke R., Dettmar R. J., Pohlen M., 2000, A&AS, 145, 405
McMillan P. J., 2017, MNRAS, 465, 76
Marino A., Bianchi L., Rampazzo R., Buson L. M., Bettoni D., 2010, A&A, 511, A29
Márquez I., Masegosa J., Moles M., Varela J., Bettoni D., Galletta G., 2002, A&A, 393, 389
Martig M., Minchev I., Ness M., Fouesneau M., Rix H.-W., 2016, ApJ, 831, 139
Martig M. et al., 2021, MNRAS, 508, 2458
Martín-Navarro I. et al., 2012, MNRAS, 427, 1102
Meng X., Gnedin O. Y., 2021, MNRAS, 502, 1433
Minchev I., Chiappini C., Martig M., 2013, A&A, 558, A9
Minchev I., Martig M., Streich D., Scannapieco C., de Jong R. S., Steinmetz M., 2015, ApJ, 804, L9
Minchev I. et al., 2019, MNRAS, 487, 3946
Muñoz-Mateos J. C. et al., 2013, ApJ, 771, 59
Nersesian A. et al., 2019, A&A, 624, A80
Nissen P. E., 2015, A&A, 579, A52
Pan Z., Li J., Lin W., Wang J., Fan L., Kong X., 2015, ApJ, 804, L42
Pérez E. et al., 2013, ApJ, 764, L1
Pinna F. et al., 2019a, A&A, 623, A19
Pinna F. et al., 2019b, A&A, 625, A95
Pipino A., Matteucci F., 2004, MNRAS, 347, 968
Pipino A., Matteucci F., Chiappini C., 2006, ApJ, 638, 739
Queiroz A. B. A. et al., 2020, A&A, 638, A76
Querejeta M. et al., 2015, ApJS, 219, 5
Quinn P. J., Hernquist L., Fullagar D. P., 1993, ApJ, 403, 74
Rahimi A., Kawata D., Allende Prieto C., Brook C. B., Gibson B. K., Kiessling A., 2011, MNRAS, 415, 1469
Robitaille T. P., Whitney B. A., 2010, ApJ, 710, L11
Ruiz-Lara T. et al., 2015, A&A, 583, A60
Sánchez-Blázquez P., Forbes D. A., Strader J., Brodie J., Proctor R., 2007, MNRAS, 377, 759
Sánchez-Blázquez P. et al., 2014, A&A, 570, A6
Sarzi M. et al., 2006, MNRAS, 366, 1151
Schawinski K. et al., 2014, MNRAS, 440, 889
Schlafly E. F., Finkbeiner D. P., 2011, ApJ, 737, 103
Schlesinger K. J. et al., 2012, ApJ, 761, 160
Schönrich R., McMillan P. J., 2017, MNRAS, 467, 1154
Scott N., van de Sande J., Sharma S., Bland-Hawthorn J., Freeman K., Gerhard O., Hayden M. R., McDermid R., 2021, ApJ, 913, L11
Sheth K. et al., 2010, PASP, 122, 1397
Skrutskie M. F. et al., 2006, AJ, 131, 1163
Tully R. B., Courtois H. M., Sorce J. G., 2016, AJ, 152, 50
van der Marel R. P., Franx M., 1993, ApJ, 407, 525
Vazdekis A., Casuso E., Peletier R. F., Beckman J. E., 1996, ApJS, 106, 307
Vazdekis A. et al., 2015, MNRAS, 449, 1177
Weilbacher P. M., Streicher O., Urrutia T., Jarno A., Pécontal-Rousset A., Bacon R., Böhm P., 2012, in Radziwill N. M., Chiozzi G.eds, Proc. SPIE Conf. Ser. Vol. 8451, Software and Cyberinfrastructure for Astronomy II. SPIE, Bellingham, p. 84510B
Wheeler A. et al., 2020, ApJ, 898, 58
Yoachim P., Dalcanton J. J., 2006, AJ, 131, 226
Yoachim P., Dalcanton J. J., 2008a, ApJ, 682, 1004
Yoachim P., Dalcanton J. J., 2008b, ApJ, 683, 707
Yu S. et al., 2021, MNRAS, 505, 889
Zhang H.-X., Hunter D. A., Elmegreen B. G., Gao Y., Schruba A., 2012, AJ, 143, 47

APPENDIX A: GAS MAPS

From the GANDALF emission line fitting, the kinematics and the fluxes of the ionized gas from the three emission lines: H β (4861.33 Å;), [O III] doublet (4958.92 & 5006.84 Å;), and [N I] doublet (5197.90 & 5200.39 Å;) were obtained.

Fig. A1 shows the fluxes of the fitted emission lines, where regions of high fluxes could be the result of some spiral arm structure with a higher star formation rate. The gas kinematic maps, presented in Fig. A2 show the mean velocity V (top maps) and velocity dispersion σ (bottom maps), measured from the emission lines. The gas kinematics of the [N I] emission line were fixed to the [O III] kinematics for the fitting with GANDALF, so the kinematics show identical results. We can see in the gas velocity maps, that the gas is overall co-rotating with the stellar material of the galaxy disc. Moreover, some pattern can be seen in the velocity dispersion, where regions of lower velocity dispersion correspond to regions of higher

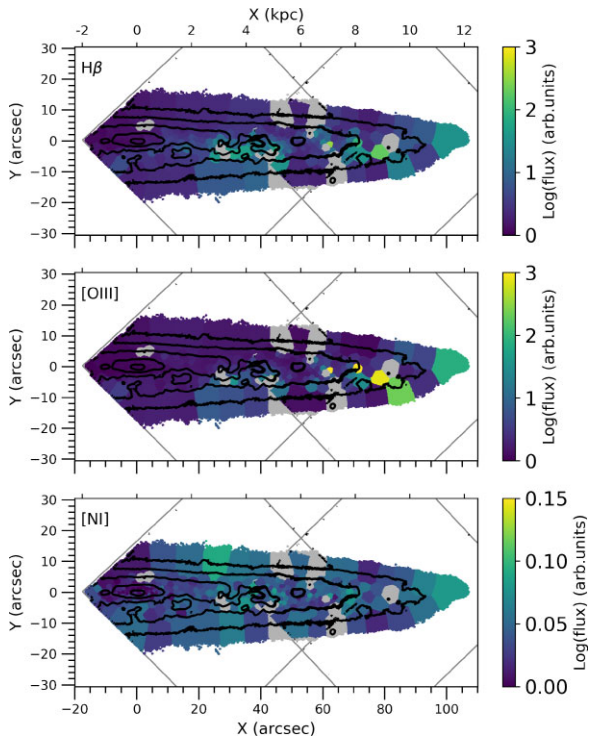

Figure A1. Flux maps of the three fitted emission lines H β, [O III], [N I] (from top to bottom). The discarded bins are plotted in grey and the approximate positions of the MUSE pointings are indicated by grey lines, while the isophotes are displayed in black.

Downloaded from https://academic.oup.com/mnras/article/520/2/3066/7008533 by guest on 17 May 2023

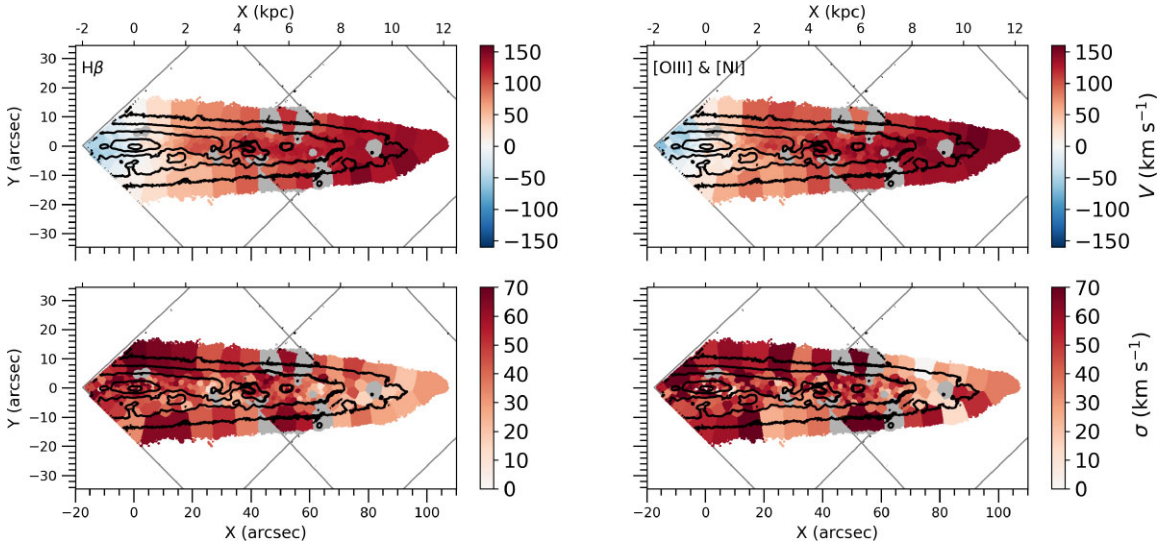

Figure A2. Kinematic maps of the ionized gas determined from fitting the emission lines H β (left), and the doublets of [O III] and [N I] (right). The mean velocity V is plotted in the top panels and the mean velocity dispersion σ in the bottom panels. The kinematics of the [N I] emission line were fixed to the [O III] kinematics, so the kinematics are the same. The discarded bins are plotted in grey and the approximate positions of the MUSE pointings are indicated by grey lines, while the isophotes are displayed in black.

flux in H β and [O III] (see Fig. A1), except for the region with high stellar velocity dispersion at ∼40 arcsec.

Performing more detailed emission line-based measurements is beyond the scope of this paper and will be done in a following project.

APPENDIX B: UNCERTAINTIES IN STELLAR KINEMATICS, STELLAR POPULATIONS, AND THE STAR FORMATION HISTORY

The uncertainties of the stellar velocity are lowest in the central mid-plane and above (∼5 km s^{-1}). In the Voronoi bins farthest away from the centre, uncertainties reach ∼30 km s^{-1}. The uncertainties of the stellar velocity dispersion show the same trend. The lowest uncertainties are found in the central region (∼10 km s^{-1}) and the highest uncertainties in the outer parts (∼50 km s^{-1}). For h_3, we find uncertainties quite as high as the values for h_3 in the central mid-plane (∼0.02). Lower uncertainties (∼0.01) are found in the outer envelope, where we also see values of h_3 oscillating close to 0. Also for h_4, uncertainties reach values of ∼0.01, while the values of h_4 are mostly of the same order, supporting the penalization of higher moments at low signal-to-noise ratio by PPXF.

From the uncertainty maps in Fig. B2, we see for youngest ages lowest statistical uncertainties (∼0.5 Gyr in the mid-plane region of the light-weighted maps) and higher uncertainties for older ages on average (∼1 Gyr in the light-weighted maps and ∼2.5 Gyr in the

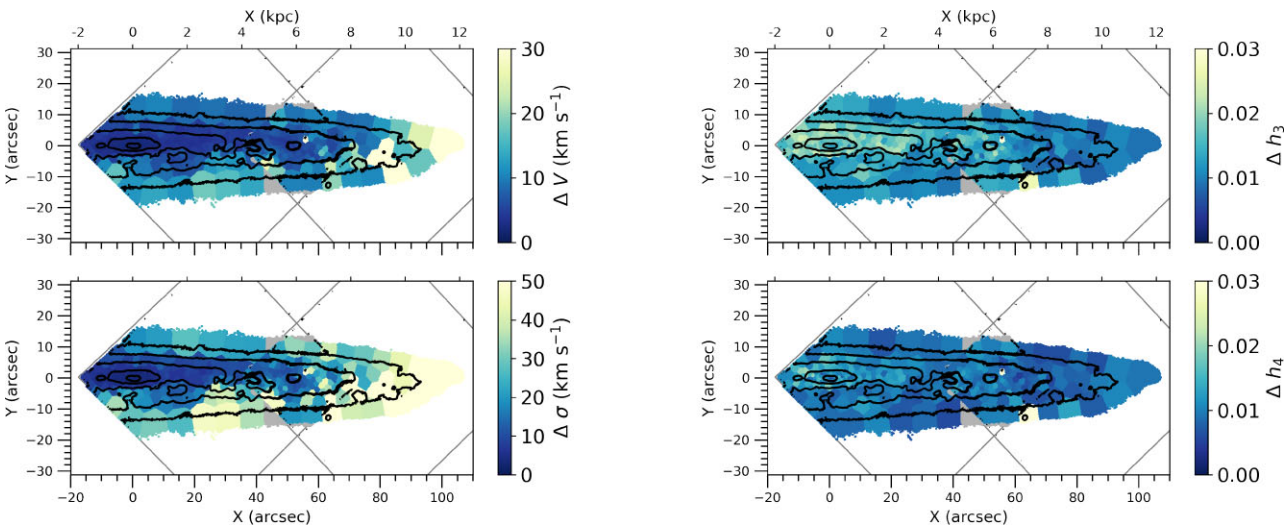

Figure B1. Left: Uncertainty maps of the velocity and velocity dispersion obtained with Monte Carlo Simulations. Right: Uncertainty maps of h_3 and h_4 obtained with Monte Carlo simulations. The approximate positions of the MUSE pointings are indicated by grey lines and the discarded bins are also displayed in grey, while the isophotes are displayed in black.

Downloaded from https://academic.oup.com/mnras/article/520/2/3066/7008533 by guest on 17 May 2023

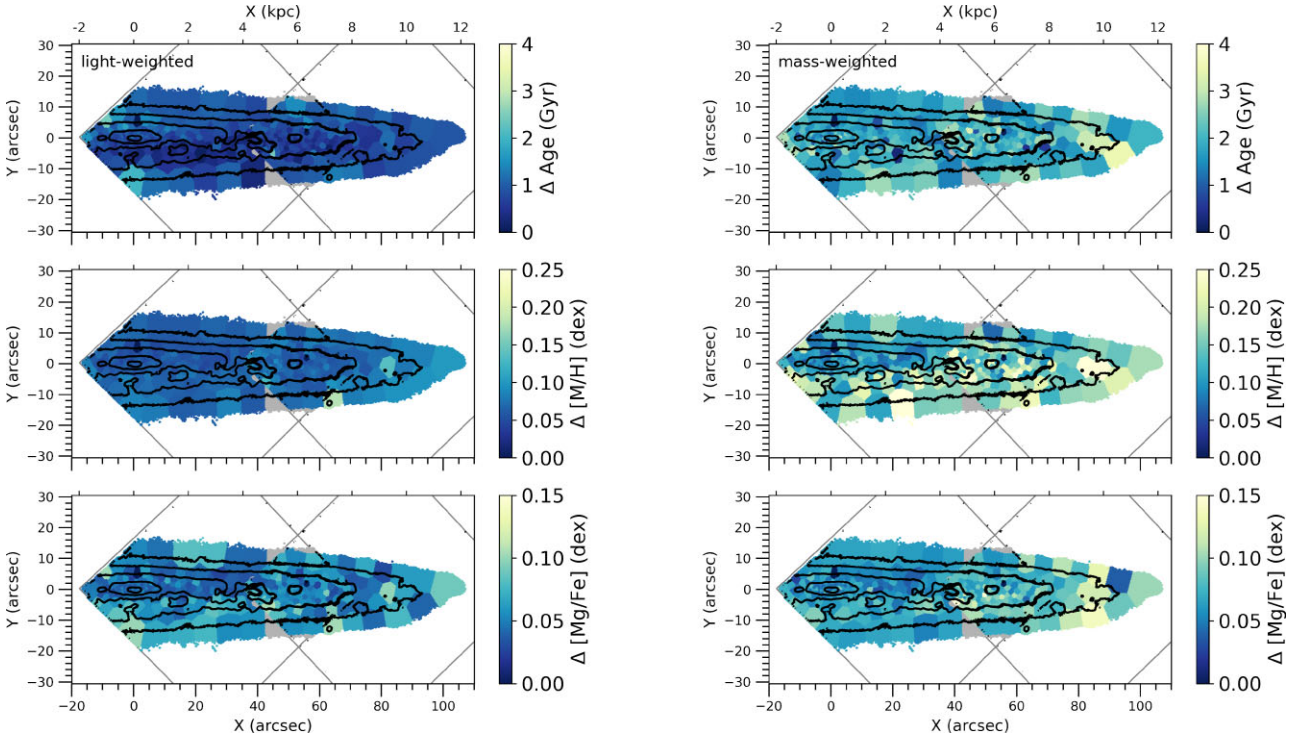

Figure B2. Uncertainty maps of the light-weighted (left) and mass-weighted (right) stellar population parameters obtained with Monte Carlo simulations. The approximate positions of the MUSE pointings are indicated by grey lines and the discarded bins are also displayed in grey, while the isophotes are displayed in black.

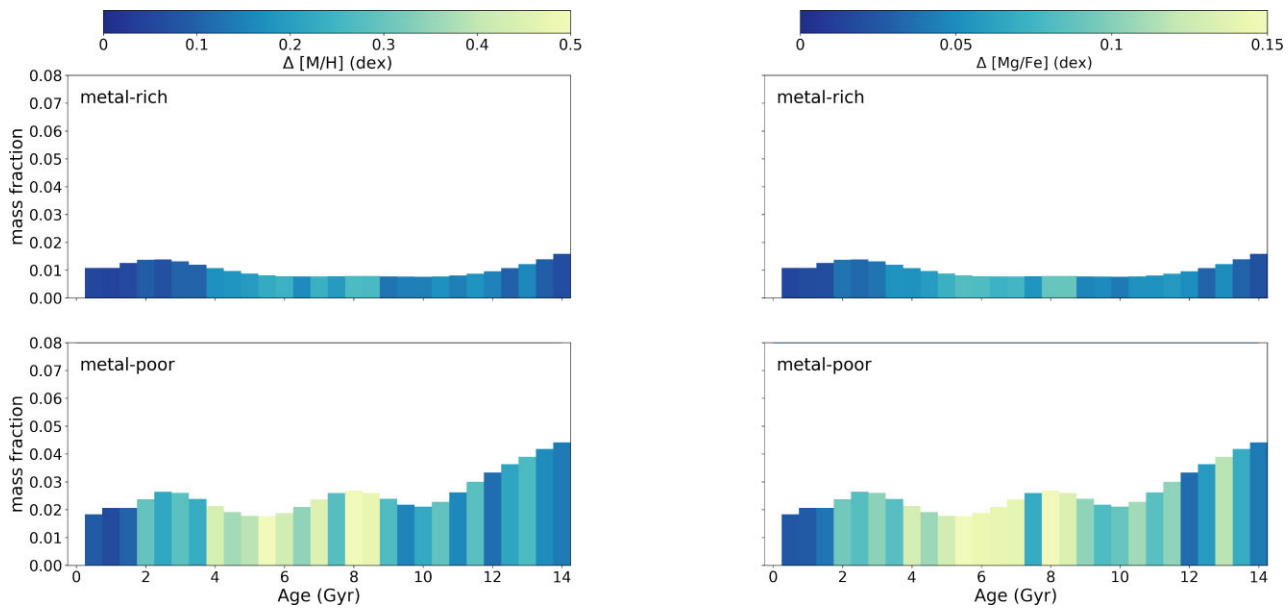

Figure B3. Uncertainties of the star formation history obtained with Monte Carlo simulations. Age bins are colour-coded by the uncertainties of metallicity [M/H] (left), and by the uncertainties of [Mg/Fe] (right). The metal-rich component is always plotted at the top, whereas the metal-poor component is always plotted at the bottom.

mass-weighted maps). The uncertainties in metallicity [M/H] (Fig. B2) are nearly constant (∼0.1 dex) over the whole galaxy half for the light-weighted results. For the mass-weighted results, uncertainties in metallicity [M/H] are lowest (∼0.1 dex) close to the central mid-plane and above and get larger (∼0.2 dex) towards the bottom of the galaxy and the outer parts. For [Mg/Fe] (Fig. B2), the uncertainties for the light-weighted results are lowest (∼0.05 dex) close to the central mid-plane and get slightly larger (∼0.1 dex) for the outer

Downloaded from https://academic.oup.com/mnras/article/520/2/3066/7008533 by guest on 17 May 2023

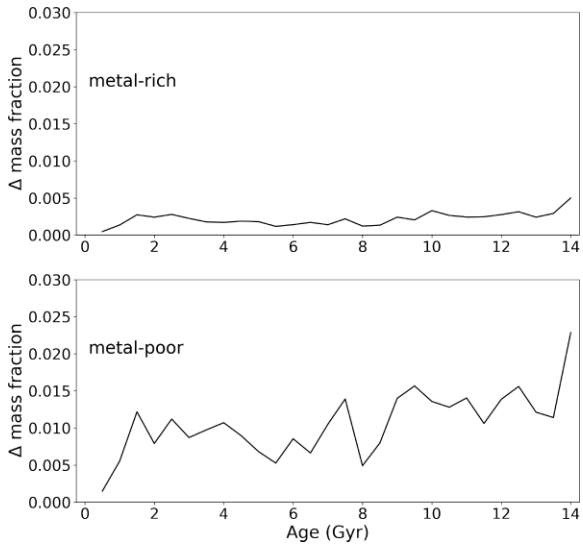

Figure B4. Uncertainties of the star formation history mass fractions obtained with Monte Carlo simulations. The metal-rich component is plotted on the top, whereas the metal-poor component is plotted at the bottom.

parts of the galaxy. For the mass-weighted results, uncertainties in [Mg/Fe] are lowest (∼0.05 dex) close to the central mid-plane, as well as above and below, and only get larger (∼0.1 dex) towards larger radii.

Using the Monte Carlo simulations, performed in Section 4.6, we calculated for each of the thousand realizations, the star formation history, and computed the standard deviation from the mean metallicity [M/H] and [Mg/Fe] values as well as the mean mass fractions to obtain an estimate of the uncertainties. Since no regularization was used in the Monte Carlo simulations, the uncertainties do not show a smooth distribution. The uncertainties for metallicity [M/H], [Mg/Fe], and the mass fractions for the star formation history are shown in Figs B3 and B4. Uncertainties in metallicity [M/H] and [Mg/Fe] (Fig. B3) as well as in mass-fractions (Fig. B4) for the metal-rich component are in general lower than for the metal-poor component, reaching ∼0.2 dex for [M/H], ∼0.1 dex for [Mg/Fe], and ∼0.003 for mass fraction. While the metal-poor component reaches higher uncertainties of ∼0.5 dex for [M/H], ∼0.15 dex for [Mg/Fe], and ∼0.015 for mass fraction. Moreover, we see lower uncertainties in metallicity [M/H] and [Mg/Fe] on average for the youngest and oldest ages in the star formation history, which tend to be more metal-rich and less enhanced in [Mg/Fe]. Those lower uncertainties reach ∼0.1 dex (∼0.2 dex) for the metal-rich (metal-poor) component in [M/H] and ∼0.05 dex (0.1 dex) for the metal-rich (metal-poor) component in [Mg/Fe]. The highest uncertainties in metallicity [M/H] and [Mg/Fe] are found for intermediate ages of 4–9 Gyr, where we find additionally lower metallicities and higher [Mg/Fe] abundances. Here, uncertainties reach ∼0.2 dex (0.4 dex) for the metal-rich (metal-poor) component in [M/H] and ∼0.1 dex (0.15 dex) for the metal-rich (metal-poor) component in [Mg/Fe].

APPENDIX C: SYSTEMATIC UNCERTAINTIES

In our procedure, we only calculated statistical uncertainties from Monte Carlo simulations (see e.g. Appendix B), which are much lower than the ones obtained in previous work using the same approach to analyse older galaxies (Pinna et al. 2019a, b; Martig et al. 2021). Models of young stellar populations show larger differences, between spectra of different ages than older models for the same age difference. Thus for young galaxies adding some noise to the spectra as we do with Monte Carlo simulations does not make PPXF change the choice of models. In young galaxies, systematic uncertainties may be dominating, but they are difficult to be quantified. We tested some of the potential sources of systematic uncertainties and we discuss them below.

To test the effect that our selection of specific MILES SSP models (Section 4.2) might have on the final results, we also fitted with PPXF all Voronoi binned spectra for stellar population parameters using the full range of ages in MILES SSP models. These include nine values for metallicity between −1.26 and 0.4 dex, to still be in the safe range of metallicity for the SSP models, but now 53 values for age going from 0.03 to 14 Gyr with a resolution between 0.01 and 0.5 Gyr and the values for [Mg/Fe] of 0.0 and 0.4 dex. With this, the main features of the star formation history (higher metallicity at old stars and a drop in metallicity, higher metallicity and [Mg/Fe] at young ages, oscillations in [Mg/Fe] and the peaks in star formation around 3, 8, 14 Gyr) were still present. So the cuts we made in age did not affect our results significantly. It also needs to be considered, that all parameters like age, metallicity, and [Mg/Fe]-abundance can be affected by the limited ranges of the SSP models. Other models might show different absolute values for the results, as discussed in several previous stellar population studies (e.g. Koleva et al. 2008; Ruiz-Lara et al. 2015; Baldwin et al. 2018; Ge et al. 2018), while the vertical and horizontal gradients, as well as the spatial coherence, would be the same when using different models.

Secondly, we fitted with PPXF all Voronoi binned spectra for stellar population parameters using different values of regularization going from 1 to 100. With this, we found that the star formation history becomes smoother for higher values of regularization and the main features of the star formation history start to get lost using a regularization higher than 10. Choosing a higher regularization than 10 gives such a smoothed-out star formation history, that oscillations in metallicity and [Mg/Fe] as well as peaks in star formation are hardly visible. On the other hand, choosing a smaller value of regularization than 10 gives a noisier star formation history with larger jumps in metallicity and [Mg/Fe]. Our choice of regularization ensures that the systematics associated with it are minimized.

Another important point is the difficulty in retrieving the [α/Fe] for young stars. For star-forming galaxies especially, the retrieval of α-enhancement is more complicated, due to relevant absorption line features being significantly weaker in those galaxies consisting of young stellar populations, than for non-star-forming galaxies consisting of older stellar populations (e.g. Conroy, Graves & van Dokkum 2014).

This paper has been typeset from a TEX/LATEX file prepared by the author.

Downloaded from https://academic.oup.com/mnras/article/520/2/3066/7008533 by guest on 17 May 2023